Giant barocaloric tunability in [(CH3CH2CH2)4N]Cd[N(CN)2]3 hybrid perovskite

Juan Manuel Bermúdez-García,a,b* Susana Yáñez-Vilar,c Alberto García-Fernández,a Manuel Sánchez-Andújar,a Socorro Castro-García,a Jorge López-Beceiro,d Ramón Artiaga,d Melony Dilshad,b Xavier Moya,b and María Antonia Señarís-Rodrígueza**

a. University of A Coruna, QuiMolMat Group, Dpt. Chemistry, Faculty of Science and Advanced Scientific Research Center (CICA), Zapateira, 15071 A Coruña, Spain.
b. University of Cambridge, Department of Materials Science and Metallurgy, Cambridge CB3 0FS, United Kingdom.
c. University of Santiago de Compostela, Dpt. Applied Physics, 15782 Santiago de Compostela, Spain.
d. University of A Coruna, Dpt. Naval and Industrial Engineering, Esteiro, 15471 Ferrol, Spain.
* j.bermudez@udc.es, **m.senaris.rodrigez@udc.es

Abstract: We report the barocaloric performance of cadmium-dicyanamide perovskite [(CH3CH2CH2)4N]Cd[N(CN)2]3 ([TPrA]Cd[dca]3). The introduction of Cd, a large second-row post-transition metal, into this hybrid organic inorganic perovskite structure leads to three separate thermally driven phase transitions and four polymorphs, which we characterize in full using temperature-dependent x-ray diffraction and temperature-dependent calorimetry. Amongst these transitions, the non-isochoric orthorhombic to tetragonal phase transition at high temperatures, with a large volume change of ~0.4%, leads to a large reversible pressure-driven isothermal change in entropy of ~11.5 J K-1 kg-1, and a giant barocaloric tunability of the transition temperature with pressure of ~38.2 K kbar-1, which are both desirable for future low-pressure barocaloric cooling applications.

1. Introduction

Hybrid organic-inorganic perovskites are an emerging family of materials with a number of attractive functional properties for e.g. applications in charge storage devices and optoelectronic devices.[1,2] These compounds, with general formula ABX_3, integrate organic and inorganic building blocks into their perovskite structure, where the A site is occupied by midsize protonated amines (e.g. $CH_3NH_3^+$, $(CH_3)_2NH_2^+$, $(CH_3)_4N^+$, $CH(NH_2)_2^+$, $C_3H_5N_2^+$, or $(CH_3CH_2CH_2)_4N^+$ = TPrA), the B site is occupied by divalent transition metal cations (e.g. Mn^{2+}, Fe^{2+}, Co^{2+}, Ni^{2+}, or Zn^{2+}), and the X site is occupied by either halides (e.g. I^-, Br^-, or Cl^-) or polyatomic bridging-bidentate ligands (e.g. N_3^-, CN^-, $HCOO^-$, SCN^-, or $N(CN)_2^-$ = dca).[1-4]

Hybrid perovskites are named according to the nature of the X-site ligand, giving rise to the groups of formate perovskites (X = $HCOO^-$)[5-22] and halide perovskites (X = I^-, Br^-, Cl^-),[23-27] which have been widely studied due to their excellent optoelectronic properties, and to the relatively less well studied groups of azide perovskites (X = N_3^-),[28-34] cyanide perovskites (X = CN^-),[35-39] thiocyanide perovskites (X = SCN^-),[40,41] dicyanometallate perovskites (X = $Au(CN)_2^-$, $Ag(CN)_2^-$)[42,43], and dicyanamide

perovskites (X = $N(CN)_2^-$).[44-52] The large choice of organic and inorganic building blocks that is available in these materials leads to rich phase diagrams with numerous crystalline structures[3], and useful properties such as highly efficient photoconversion[2] and (type-I/type-II) multiferroicity[1].

In the last decade, dicyanamide perovskites $AB[dca]_3$ have therefore attracted growing attention not only because of their optoelectronic[50,51] and multiferroic properties,[44-48] but also because of the existence of multiple structural phase transitions that are primarily associated with the order and the off-centre displacement of their organic cations and inorganic anions. However, only very recently[52,53] these hybrid perovskites have been proposed for eco-friendly barocaloric cooling applications.[54-57] Here we synthesize a new $[TPrA]Cd[dca]_3$ cadmium-dicyanamide perovskite and investigate its barocaloric properties. Near its orthorhombic to tetragonal first-order phase transition at transition temperature T_t ~ 385 K, we find large isothermal changes in entropy $|\Delta S|$ of ~11.5 J K^{-1} kg^{-1} that can be driven reversibly using very low changes in applied pressure p of $|\Delta p| = |p - p_{atm}| \sim |p| \sim 0.07$ kbar (p_{atm} is atmospheric pressure), which are similar to the driving pressures used in existing vapour-compression refrigerators and air-conditioners.[58] This is because the high-temperature first-order structural transition in our hybrid perovskite is (i) very sharp and low hysteretic, and (ii) easily tunable with pressure. Giant barocaloric tunabilities of sharp nominally unhysteretic first-order phase transitions with large latent heats could therefore contribute to the future development of cooling devices with low driving pressures and high frequencies of operation.

2. Experimental

Caution! *Compounds containing cadmium are highly toxic. Care must be taken when handling and disposing these compounds.*

2.1 Sample synthesis

$[TPrA]Cd[dca]_3$ was prepared using as-purchased commercially available $Cd(NO_3)_2{\cdot}4H_2O$ (98%, Sigma-Aldrich), (TPrA)Br (98%, Sigma-Aldrich), Na(dca) (96%, Sigma-Aldrich) and absolute ethanol (Panreac), all without further purification, and deionised water. We followed a similar synthesis route to that previously used[46-48] in the preparation of related $[TPrA]M[dca]_3$ hybrid perovskites with M = Mn^{2+}, Fe^{2+}, Co^{2+} and Ni^{2+}, where the synthesis of the metal dicyanamide framework was templated by alkylammonium cations, and achieved at room temperature via mild-solution chemistry. In a typical synthesis, 10 ml of an aqueous solution containing 2 mmol of $Cd(NO_3)_2{\cdot}4H_2O$ was placed in a glass tube, followed by a mixture of a solution of 2 mmol of (TPrA)Br in 10 ml of ethanol, and a solution of 6mmol of Na(dca) in 10 ml of water. The resulting layered solution was left to rest for one week for the reaction to be completed, and then single crystals of $[TPrA]Cd[dca]_3$ in the shape of colourless cubes were collected by filtration, and ultimately washed several times with ethanol.

2.2 Single-crystal x-ray diffraction

Single-crystal x-ray diffraction was performed using a Bruker-Nonius x8 ApexII diffractometer equipped with a CCD detector, using monochromatic Mo $K_{\alpha 1}$ = 0.71073 Å radiation. Data were taken on cooling at 390 K, 368 K, 300 K, 200 K, and 100 K. Sample temperature was controlled using a cold stream of nitrogen from a Kyroflex

cryostream cooler. The recorded x-ray intensity was corrected for both Lorentz and polarization factors and for absorption using semi-empirical methods based on symmetry-equivalent data, using 2004 SADABS software. Data analysis was performed using Apex2 V.1.0 27 software (Bruker-Nonius, 2005). Crystalline structures were initially determined by direct methods[59] based on the observed intensities, and then refined by full-matrix least-squares methods, using SHELXS-97 software tools[60] that are available within the WinGX software package.[61] For ordered C, N and Cd atoms, anisotropic thermal factors were employed. For partially ordered TPrA cations, H atoms in the propyl groups ($CH_3CH_2CH_2$) were first located at their ideal positions, and then their isotropic thermal factors were refined. For highly disordered TPrA cations, we did not determine the location of the H atoms in the propyl groups.

2.3 Powder x-ray diffraction

Room-temperature powder x-ray diffraction was performed using a Siemens D-5000 diffractometer using Cu K_α = 1.5418 Å radiation. Sample purity was determined from x-ray datasets using Le Bail method.[62]

Temperature-dependent powder x-ray diffraction was performed using a D8 Advance Bruker powder diffractometer using Cu K_α = 1.5406 Å radiation. [TPrA]Cd[dca]$_3$ samples were placed on top of a sheet of amorphous silicon, and then mounted on an alumina (Al_2O_3) sample holder that was inserted into a modular dome-type temperature chamber, where temperature can be varied between 300 K and 430 K. Before each dataset was taken, sample temperature was increased at 0.3 K s^{-1} to the measurement temperature and then stabilised for 60 s. Diffraction patterns were collected over the 2θ range 7.5° to 30° using a VÅNTEC-1 fast detector, with a step size of 0.03° and a holding time of 3 s per step.

2.4 Differential scanning calorimetry

Differential scanning calorimetry at atmospheric pressure was performed using a TA Instruments MDSC Q2000, equipped with a liquid nitrogen cooling system. For these measurements, [TPrA]Cd[dca]$_3$ samples of ~5 mg were scanned between 200 K and 425 K, using heating and cooling rates of 20 K min^{-1}.

Variable-pressure differential scanning calorimetry was performed in the same TA Instruments calorimeter, with a pressure cell add-on that permits operation between atmospheric pressure and ~0.07 kbar, using nitrogen as pressure transmitting medium. Temperature and heat flow readings were calibrated using samples of indium, for which the effect of pressure on melting temperature and latent heat of fusion is well known.[63,64] For these measurements, [TPrA]Cd[dca]$_3$ samples of ~5 mg were inserted inside pinhole aluminium capsules, and then scanned between 370 K and 400 K, using heating and cooling rates of 2 K min^{-1}.

2.5 Thermogravimetric analysis

Thermogravimetric analysis was performed in a TA Instruments SDT 2960 Simultaneous DSC-TGA, using [TPrA]Cd[dca]$_3$ samples of ~25 mg, corundum crucibles, and heating rates of 5 K min^{-1} from 298 K to 1173 K, under a flow of dry nitrogen.

3. Results and discussion

Room-temperature powder x-ray diffraction (Figure 1) confirmed that our samples are single-phase perovskites, despite the introduction of a large second-row post-transition metal in the B site (ionic radii: ${}^{\mathbf{VI}}r_{Cd^{2+}} = 0.95$ Å > ${}^{\mathbf{VI}}r_{(Mn^{2+})HS} = 0.83$ Å > ${}^{\mathbf{VI}}r_{(Fe^{2+})HS} = 0.78$ Å > ${}^{\mathbf{VI}}r_{(Co^{2+})HS} = 0.745$ Å > ${}^{\mathbf{VI}}r_{Ni^{2+}} = 0.69$ Å; HS = high-spin configuration).[65] Thermogravimetric analysis confirmed that the samples are stable up to 513 K (Figure S1 of SI).

3.1 Thermally driven phase transitions in [TPrA]Cd[dca]$_3$

Calorimetry at atmospheric pressure (Figure 2) revealed that [TPrA]Cd[dca]$_3$ undergoes three separate thermally driven first-order phase transitions within the temperature range 200 - 425 K, similarly to related Fe-, Co- and Ni-dicyanamides perovskites.[48] The transition temperatures, identified using the peaks in heat flow on heating (T_{h1}, T_{h2} and T_{h3}) and on cooling (T_{c1}, T_{c2} and T_{c3}) are summarized in Table 1, alongside the corresponding changes in entropy and latent heats, which were obtained via suitable integration of the peaks in heat flow.[54,66,67]

The ratio between the number of configurations in disordered phases and ordered phases, N, can be estimated via the expression $\Delta S = R \ln(N)$, which is widely used in the literature for hybrid materials (R is the universal gas constant). Our calculated values for N, which vary between 1 and 2.6, are similar to the values calculated for Fe-, Co- and Ni-dicyanamide perovskites, but smaller than that estimated for [TPrA]Mn[dca]$_3$, which displays only one thermally driven first-order phase transition[47] with $N \sim 8$.

3.2 Polymorphic crystal structure

Below, we describe the main structural properties of the four polymorphs observed in our [TPrA]Cd[dca]$_3$ perovskite. The full crystallographic information is summarised in Tables S1-S4 of ESI.

Polymorph 0, P0. At low temperatures (T < 240 K), our Cd-dicyanamide perovskite displays a crystal structure that has not been hitherto observed in other members of the [TPrA]M[dca]$_3$ family, namely a monoclinic structure with P2$_1$/n space group, which is centrosymmetric (Table S1 of ESI).

The asymmetric unit (i.e. the motif) contains two metal cations, six different dca inorganic anions, and two different TPrA organic cations. Each Cd^{2+} cation is in a distorted CdN_6^- octahedral environment with six different Cd-N distances (Table S2 of ESI). The P0 crystalline structure is almost completely ordered, as only one of the TPrA cations located inside the cavities of the Cd[dca]$_3^-$ framework exhibits slight disordering in two of its propyl groups (Figure 3). We note that within the [TPrA]M[dca]$_3$ family, this high degree of ordering is unique to this polymorph.

Also, the TPrA cations show ~0.19 Å off-centre displacements towards one of the corners of the pseudocuboctahedral cavity, which almost doubles the ~0.11 Å displacement observed in [TPrA]Mn[dca]$_3$ at low temperatures. These off-centre displacements are related to columnar shifts that are out-of-phase[4] and active along the a and c axis, but inactive along the b axis (Figure 4), which leads to the antiparallel arrangement of the TPrA displacements along this b axis (Figure S2 of ESI).

Polymorph I, PI. Between 240 K < T < 360 K, there is an increase in the structural disordering, and this leads to a different structure (Figure 5). The resulting polymorph PI, which is also observed in Mn-, Fe-, Co- and Ni-dicyanamide perovskites,[47,48] displays tetragonal symmetry with space group $P\bar{4}2_1c$, which is non-centrosymmetric (Table S1 of SI).

For this polymorph, the asymmetric unit is defined by one metal cation, three dca anions, and three TPrA cations, where the metal cation is still in a distorted octahedral environment with six different Cd-N distances (Table S3 of ESI).

When compared to the polymorph P0, the polymorph PI displays a large disorder in the C atoms that are present in two of the three TPrA cations, and a smaller disorder in the dca anions, where the N atoms at their centre, which are bonded to C atoms, i.e. the N-amide atoms, are partially disordered along the *c* axis and in the *ab* plane. Also, half of the TPrA cations are now located in the centre of the pseudocuboctahedral cavities, while the other half remain arranged in an antiferrodistorsive up-down pattern along the *c* axis (Figure S3). While the off-centre displacements of the TPrA cations in the polymorph PI (~0.123 Å) are smaller than those in P0, they are larger than the off-centre displacements observed in the PI polymorphs of other dicyanamide perovskites (~0.105 Å for M = Mn, ~0.095 Å for M = Fe, ~0.069 Å for M = Co, and ~0.038 Å for M = Ni).

An interesting feature that has been hitherto not noticed in previous reports of PI polymorphs in dicyanamide perovskites[47,48] is that the off-centre TPrA displacements are also associated with active columnar shifts, as in the polymorph P0. Therefore, when the Cd-dicyanamide perovskite transforms from P0 to PI, there is an activation of columnar shifts along the *b* axis, which leads to out-of-phase columnar shifts along all three crystallographic axes (Figure S4 of ESI).

Polymorph Ib, PIb. The presence of pseudo-merohedral twinning in our analysed single crystals, along with the presence of increased structural disorder, prevented us from resolving the crystal structure of this polymorph via single- crystal x-ray diffraction. Nevertheless, Le Bail refinement of the powder x-ray pattern obtained at 380 K (Figure S5 of ESI) revealed that PIb displays orthorhombic symmetry with *Ibam* space group, which is centrosymmetric (Table S1 of ESI). This space group is the same to that observed in the polymorphs PIb of Fe-, Co- and Ni-dicyanamide perovskites, where all the TPrA cations are centred in the pseudocuboctahedral cavities, all the columnar shifts are inactive, and the TPrA and the dca ions are slightly more disordered than in their corresponding polymorphs PI. [48]

Polymorph II, PII. At high temperatures, the structural disorder in $[TPrA]Cd[dca]_3$ increases significantly and the compound undergoes a phase transition towards a tetragonal phase with space group *I4/mcm*, which is yet again centrosymmetric (Table S1). As shown in Figure 6, the disorder in the N-amide atoms and C atoms that are present in the dca ligands is very large, making these ligands to be seemingly acting as rotors along the *c* axis.

Separately, the TPrA cations in this polymorph, whose propyl groups are also highly disordered, remain centred in the cavities, and their columnar shifts remain inactive

along the three crystallographic axes. However, it should be noted that the PII structure in our Cd perovskite exhibits relatively less disorder than the same polymorph in the related Mn, Fe, Co and Ni perovskites.[47,48]

Phase diagram. Using our room-temperature single-crystal x-ray diffraction data, we estimated the tolerance factor[68,69] for the [TPrA]Cd[dca]$_3$ perovskite as $t = (r_A+r_X)/\sqrt{2}(r_B+0.5h_X) = 1.00$ (h_x is the effective height of dca). Our calculated value is the smallest tolerance factor for [TPrA]M[dca]$_3$, due to the larger ionic radius of Cd^{2+} with respect to other B-site cations (t(Cd-perovskite) = 1.00 < t(Mn-perovskite) = 1.02 < t(Fe-perovskite) = 1.03 < t(Co-perovskite) = 1.04 < t(Ni-perovskite) = 1.05).[48]

Using these calculated values, we compare in Figure 7 the relative thermal stability of the different polymorphs in our Cd perovskite with that of the polymorphs present in the other members of the [TPrA]M[dca]$_3$ family (M = Mn^{2+}, Fe^{2+}, Co^{2+} and Ni^{2+}), with respect to values of the tolerance factor (and therefore M ionic radii). The Mn-dicyanamide perovskite has only two polymorphs, PI and PII, whereas the Fe-, Co- and Ni-dicyanamide perovskites - with t > t(Mn-perovskite) - have four different polymorphs, PI, PIa, PIb, and PII.[47,48] The Cd- dicyanamide perovskite - with t < t(Mn-perovskite) - has also four different polymorphs, but in this case P0, PI, PIb, PII.

Therefore, it is apparent that changes in tolerance factor in hybrid organic-inorganic perovskites lead to different sequences of phase transitions, different polymorphs, and also different transition temperatures (other factors that may influence these phase transitions include octahedral factor, ionic electronegativity and covalent bond character[70]). It is also apparent that the Mn-dicyanamide perovskite shows an ideal tolerance factor that minimizes strain and therefore the number of polymorphs available.

3.2 Barocaloric properties

Large changes in ionic order at first-order phase transitions can lead to large changes in entropy and large changes in volume, which are both attractive for barocaloric applications.

We therefore performed quasi-direct measurements[54] of barocaloric effects near the T_t ~ 385 K orthorhombic to tetragonal phase transition (Figure 8), which displays the largest thermally driven change in entropy and latent heat for this Cd-dicyanamide perovskite (Table 1).

On increasing the applied pressure, there is a shift of the transition towards higher temperatures. The corresponding barocaloric tunability for the transition $|dT_t/dp|$ = 38.2 K kbar^{-1} is giant and exceeds the values observed in state-of-the-art barocaloric materials[52,66,67,71-76] (Table 2 and Figure 9).

Our experimental value of the barocaloric tunability is in good agreement with the 33.0 K kbar^{-1} value estimated using the Clausius-Clapeyron relation:[54]

$$\left|\frac{dT_t}{dp}\right| = \frac{|\Delta V_t|}{|\Delta S_t|}$$

where $|\Delta V_t|$ ~ 5.3 x 10^{-6} m^3 kg^{-1} is the change in specific volume at the phase transition, which represents a relative change of ~0.4%, and which was determined using our variable-temperature powder x-ray diffraction data (Figure S6 of ESI).

We calculated barocaloric isothermal changes in entropy from our quasi-direct measurements, by first taking the difference between thermally driven changes in entropy measured at two different pressures, and then adding the additional changes in isothermal entropy that arise due to the volumetric thermal expansion either side of the transition (Figure S6 of ESI), as explained first in reference 66. Following this method, we found large isothermal changes in entropy $|\Delta S|$ of ~11.5 J K^{-1} kg^{-1} that can be driven reversibly using very low changes in applied pressure of ~0.07 kbar.

The large barocaloric entropy changes in our [TPrA]Cd[dca]$_3$ perovskite arise because the changes in the degree of ordering of the TPrA cations and dca ligands are large at the pressure-driven PIb-PII phase transition (as the large value of N in Table 1 indicates), and the large barocaloric tunability arises because the concomitant changes in the positions of these ions lead to large changes in volume.

The low driving pressures arise because the first-order structural transition in our [TPrA]Cd[dca]$_3$ perovskite is very sharp (1 K wide), low hysteretic (T_{h3} - T_{c3} = 1.4 K), and easily tunable with pressure ($|dT_t/dp|$ = 38.2 K $kbar^{-1}$) [Table 2].

Conclusions

We synthesised a [TPrA]Cd[dca]$_3$ hybrid organic-inorganic perovskite, where the introduction of Cd^{2+} into the B-site position leads to three separate thermally driven phase transitions and four polymorphs. Our newly synthesised compound displays a number of interesting structural properties, such as (i) the presence of a highly ordered polymorph at low temperatures, which has not been hitherto observed in [TPrA]M[dca]$_3$ perovskites, (ii) the presence of large columnar shifts, (iii) the disappearance of the intermediate polymorph PIa, which has been previously observed in Fe-, Co- and Ni-dicyanamide perovskites, and (iv) the re-entry of the intermediate polymorph PIb, between the polymorphs PI and PII, upon increasing the ionic radii of the B-site cation from Mn^{2+} to Cd^{2+}.

Amongst the three observed phase transitions, the non-isochoric orthorhombic to tetragonal phase transition at ~385 K, with a volume change of ~0.4%, is highly tunable with pressure and yields large reversible barocaloric changes in entropy that are driven using very low changes in applied pressure. This is because of the large pressure-driven changes in both position and degree of ordering of the different ions that make this hybrid organic-inorganic perovskite.

Our work should inspire the development of materials with giant values of barocaloric tunability, which should ultimately lead to barocaloric coolers that operate at pressures and frequencies that are similar to those used in commercial vapour-compression refrigerators and air-conditioners.

Conflicts of interest

There are no conflicts of interest to declare.

Acknowledgements

We thank Dr E. Stern-Taulats, Dr G. Nataf and Mr A. Avramenko for useful discussions about barocalorics. The authors are grateful for financial support from Ministerio de Economía y Competitividad MINECO and EU-FEDER (project MAT2017-86453-R), and ERC Starting Grant no 680032. J.M.B.G. acknowledges Xunta de Galicia for a Postdoctoral Fellowship. X.M. is grateful for support from the Royal Society.

Figures

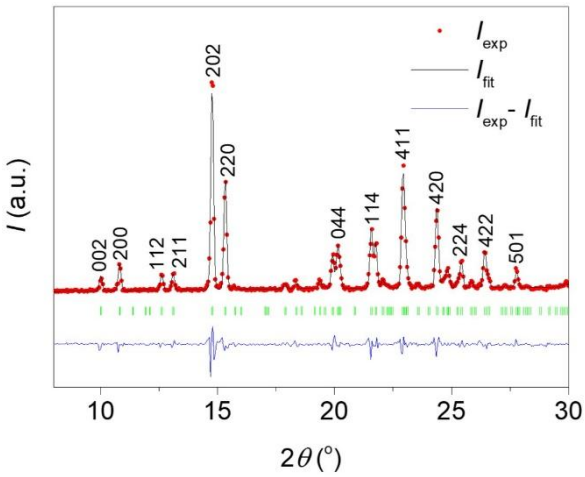

Figure 1. Room-temperature Le Bail refinement of x-ray powder diffraction data. Red symbols are experimental data, black lines are fitted patterns, green lines indicate indexed reflections.

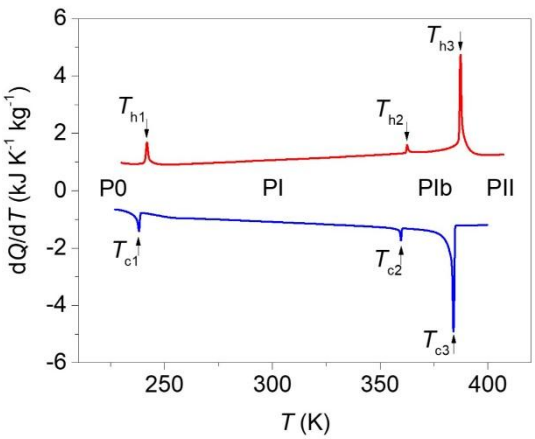

Figure 2. Heat flow as a function of temperature, at atmospheric pressure. P0, PI, PIb and PII represent the four different polymorphs observed in [TPrA]Cd[dca]$_3$.

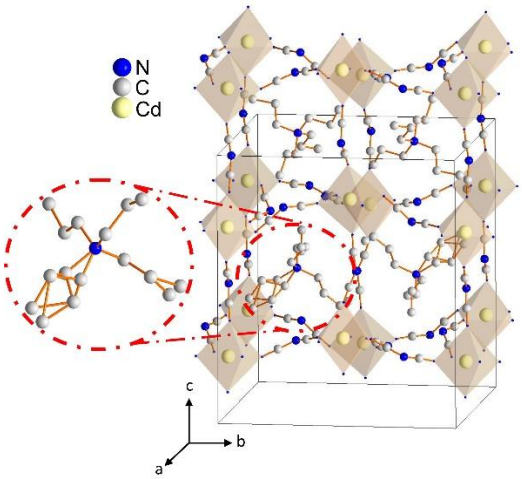

Figure 3. P0 crystal structure, with unit cell shown using grey lines. dca ligands act as $\mu_{1\text{-}5}$ bridges between Cd^{2+} cations. TPrA cations are located inside pseudocuboctahedral cavities, and show partial disordering of the C atoms (enlarged detail within red lines). H atoms at the TPrA cations are omitted for clarity of visualisation.

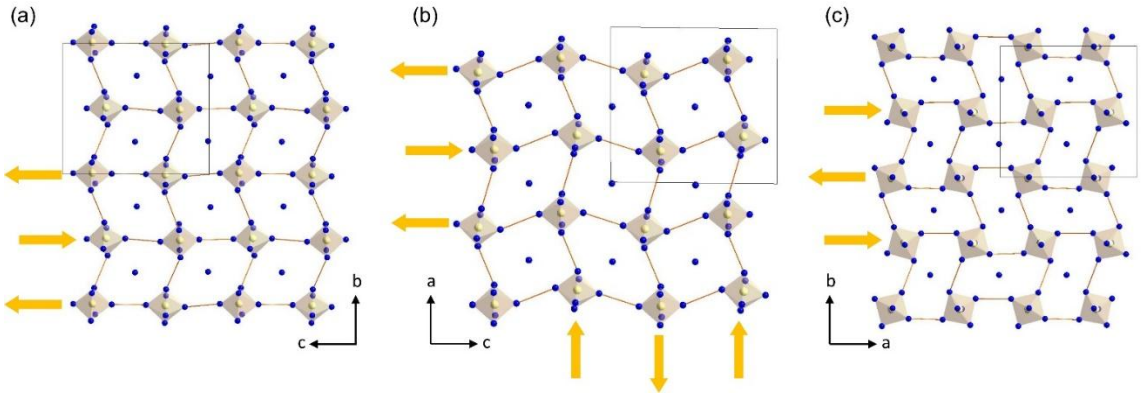

Figure 4. Columnar shifts present in the polymorph P0, represented using plane views along (a) the *a* axis, (b) the *b* axis, and (c) the *c* axis. Columnar shifts are active and out-of-phase along the *a* axis and *c* axis, as indicated by the yellow arrows, whereas they are inactive along the *b* axis. Projected unit cells are shown using bue lines.

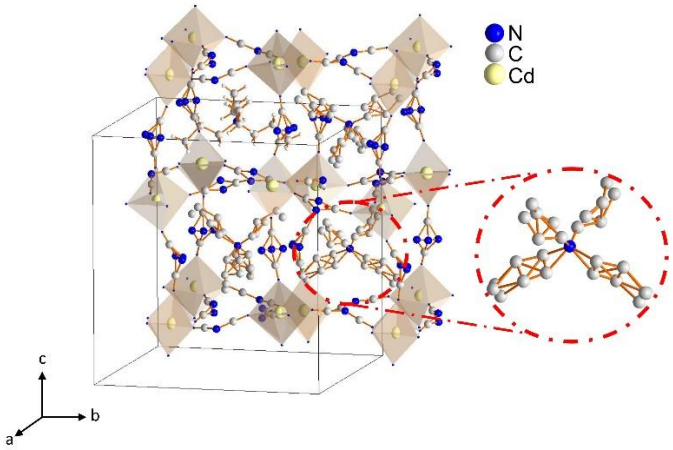

Figure 5. PI crystal structure, with unit cell shown using grey lines. dca ligands act as $\mu_{1\text{-}5}$ bridges between Cd^{2+} cations. N-amide atoms belonging to the dca ligands are shown in two different crystallographic positions when the dca ligand lies in the a-b plane, and in three different crystallographic positions when the dca ligand lies along the *c* axis. TPrA cations, which are located inside pseudocuboctahedral cavities, show higher disordering of the C atoms (enlarged detail within red lines) with respect to the P0 polymorph. H atoms at the TPrA cations are omitted for clarity of visualisation.

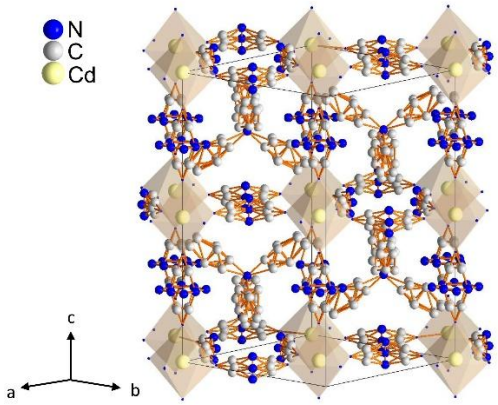

Figure 6. PII crystal structure, with unit cell shown using grey lines. N-amide atoms and C atoms belonging to the dca ligands are shown in three different crystallographic positions when the dca ligand lies in the a-b plane, and in eight different crystallographic positions (for N-amide) and four different crystallographic positions (for C) when the dca ligand lies along the *c* axis. All the TPrA cations show high disordering of the C atoms. H atoms in the TPrA propyl groups are not shown because we did not determine their positions for this highly disordered polymorph.

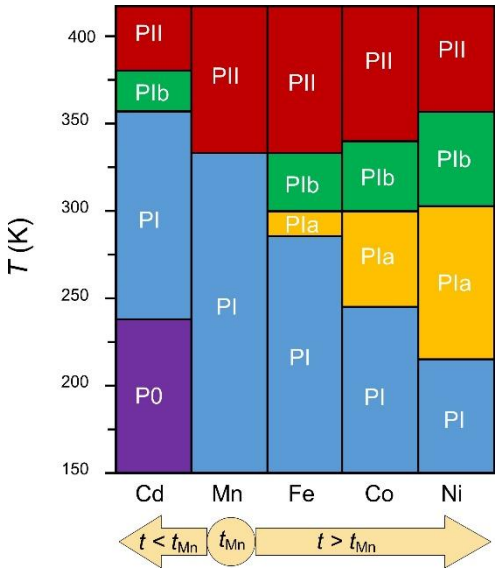

Figure 7. Schematic phase diagram of [TPrA]M[dca]$_3$ perovskites (M = Cd^{2+}, Mn^{2+}, Fe^{2+}, Co^{2+} and Ni^{2+}). Ionic radii decreases from left to right, room-temperature tolerance factor *t* decreases from right to left. t_{Mn} represents the ideal tolerance factor for the Mn-dicyanamide perovskite.

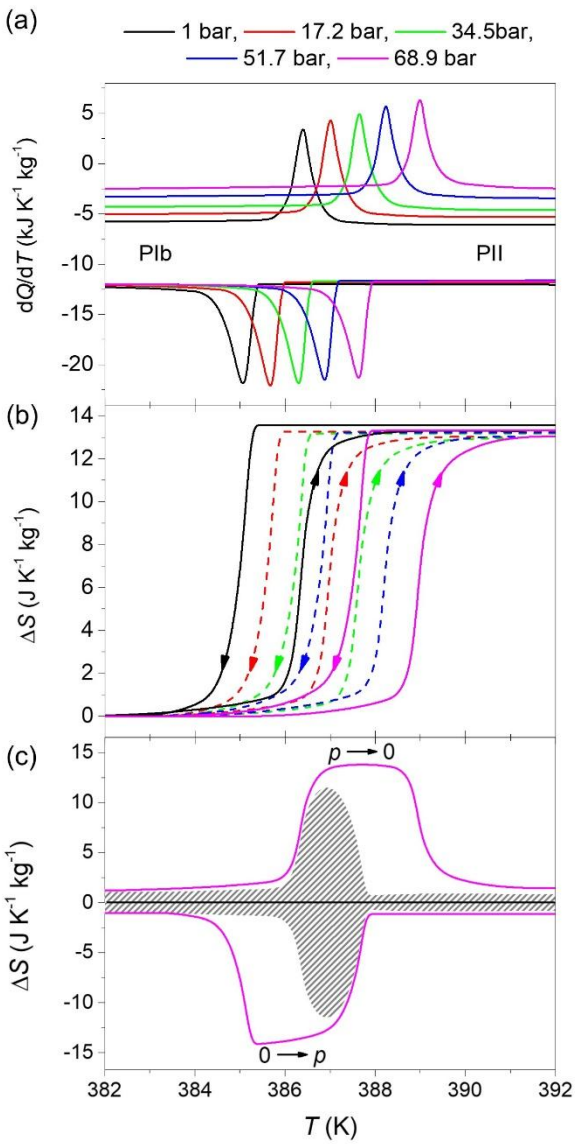

Figure 8. (a) Heat flow as a function of temperature at finite pressures. PIb and PII represent the two polymorphs of interest. (b) Thermally driven isobaric changes in entropy on heating (upward arrows) and on cooling (downward arrows), with respect to the low-temperature phase for each pressure. (c) Pressure-driven isothermal changes in entropy on applying (0→p) and removing (p→0) the maximum available pressure of ~0.07 kbar. The data shaded in grey represent the reversible barocaloric response, as explained in reference 67.

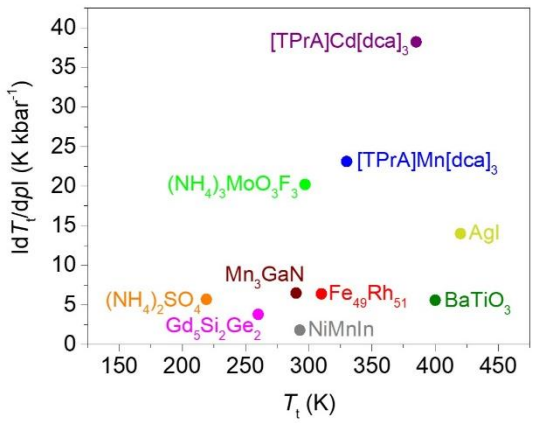

Figure 9. Barocaloric tunability for state-of-the-art giant barocaloric materials.

Table 1. Structural transition temperatures T_t, latent heats $|Q_t|$ and corresponding changes in entropy $|\Delta S_t| = |Q_t|/T_t$ for the three thermally driven phase transitions seen in [TPrA]Cd[dca]$_3$. Average values for the ratio between the number of configurations available in the different phases are given at the bottom of the table.

	Heating			**Cooling**		
	T_{h1}	T_{h2}	T_{h3}	T_{c1}	T_{c2}	T_{c3}
T_t (K)	242	363	387	238	360	384
$\|Q_t\|$ (kJ kg^{-1})	1.2	0.3	5.7	1.5	0.3	6.7
$\|\Delta S_t\|$ (J K^{-1} kg^{-1})	5.0	0.8	14.9	6.2	0.9	17.5

	P0 - PI	**PI - PIb**	**PIb - PII**
N	1.4	1.0	2.6

Table 2. Structural transition temperature T_t, latent heat $|Q_t|$ and barocaloric tunability $|dT_t/dp|$ for state-of-the-art barocaloric materials that have been studied using quasi-direct methods.

Barocaloric material	T_t **(K)**	Q_t **(kJ kg^{-1})**	$\|dT_t/dp\|$ **(K kbar^{-1})**	**Ref.**
Mn_3GaN	290	6.29	6.5	[71]
$Ni_{49.26}Mn_{36.08}In_{14.66}$	293	7.91	1.8	[72]
$Gd_5Si_2Ge_2$	260	5.46	3.8	[73]
$Fe_{49}Rh_{51}$	310	3.90	6.4	[74]
$BaTiO_3$	400	0.96	5.6	[75]
$(NH_4)_2SO_4$	219	14.50	5.7	[66]
$(NH_4)_3MoO_3F_3$	297	14.90	20.2	[76]
AgI	420	26.88	14.0	[67]
$[TPrA]Mn[dca]_3$	330	14.03	23.1	[52]
$[TPrA]Cd[dca]_3$	385	6.23	38.2	This work

Notes and references

B. Saparov and D. B. Mitzi, *Chem. Rev.*, 2016, **116**, 4558.

Y. Zhao and K. Zhu, *Chem. Soc. Rev.*, 2016, **45**, 655.

W.-J. Xu, Z.-Y. Du, W.-X. Zhang and X.-M. Chen, *CrystEngComm.*, 2016, **18**, 7915.

H. L. B. Boström, J. A. Hill and A. L. Goodwin, *Phys. Chem. Chem. Phys.*, 2016, **18**, 31881.

P. Jain, N. S. Dalal, B. H. Toby, H. W. Kroto and A. K. Cheetham, *J. Am. Chem. Soc.*, 2008, **130**, 10450.

P. Jain, V. Ramachandran, R. J. Clark, H. D. Zhou, B. H. Toby, N. S. Dalal, H. W. Kroto and A. K. Cheetham, *J. Am. Chem. Soc.*, 2009, **131**, 13625.

M. Sánchez-Andújar, S. Presedo, S. Yáñez-Vilar, S. Castro-García, J. Shamir and M. A. Señarís-Rodríguez, *Inorg. Chem.*, 2010, **49**, 1510.

Z. Zhang, W. Li, M. A. Carpenter, C. J. Howard and A. K. Cheetham, *CrystEngComm.*, 2015, **17**, 370.

I. E. Collings, J. A. Hill, A. B. Cairns, R. I. Cooper, A. L. Thompson, J. E. Parker, C. C. Tang and A. L. Goodwin, *Dalton Trans.*, 2016, **45**, 4169.

N. L. Evans, P. M. M. Thygesen, H. L. B. Boström, E. M. Reynolds, I. E. Collings, A. E. Phillips and A. L. Goodwin, *J. Am. Chem. Soc.*, 2016, **138**, 9393.

G. Kieslich, S. Kumagai, K. T. Butler, T. Okamura, C. H. Hendon, S. Sun, M. Yamashita, A. Walsh and A. K. Cheetham, *Chem. Commun.*, 2015, **51**, 15538.

S. Chen, R. Shang, K.-L. Hu, Z.-M. Wang and S. Gao, *Inorg. Chem. Front.*, 2014, **1**, 83.

S. Chen, R. Shang, B.-W. Wang, Z.-M. Wang and S. Gao, *Angew. Chem. Int. Ed.*, 2015, **127**, 11245.

R. Shang, S. Chen, B.-W. Wang, Z.-M. Wang and S. Gao, *Angew. Chem. Int. Ed.*, 2016, **55**, 2097.

B. Zhou, Y. Imai, A. Kobayashi, Z.-M. Wang and H. Kobayashi, *Angew. Chem. Int. Ed. Engl.*, 2011, **50**, 11441.

Y. Imai, B. Zhou, Y. Ito, H. Fijimori, A. Kobayashi, Z. M. Wang and H. Kobayashi, *Chem. Asian J.*, 2012, **7**, 2786.

M. Ptak, M. Maczka, A. Gagor, A. Sieradzki, A. Stroppa, D. Di Sante, M. J. Perez-Mato and L. Macalik, *Dalton Trans.*, 2016, **45**, 2574.

M. Maczka, A. Gagor, M. Ptak, W. Paraguassu, T. Almeida da Silva, A. Sieradzki and A. Pikul, *Chem. Mater.*, 2017, **29**, 2264.

L. Xin, Z. Fan, G. Li, M. Zhang, Y. Han, J. Wang, K. P. Ong, L. Qin, Y. Zheng and X. Lou, *New J. Chem.*, 2017, **41**, 151.

A. Stroppa, P. Barone, P. Jain, J. M. Perez-Mato and S. Picozzi, *Adv. Mater.*, 2013, **25**, 2284.

P. Jain, A. Stroppa, D. Nabok, A. Marino, A. Rubano, D. Paparo, M. Matsubara, H. Nakotte, M. Fiebig, S. Picozzi, E. S. Choi, A. K. Cheetham, C. Draxl, N. S Dalal and V. S Zapf, *npj Quantum Materials*, 2016, **1**, 16012.

L. C. Gómez-Aguirre, B. Pato-Doldán, J. Mira, S. Castro-García, M. A. Señarís-Rodríguez, M. Sánchez-Andújar, J. Singleton and V. S. Zapf, *J. Am. Chem. Soc.*, 2016, **138**, 1122.

J. Burschka, N. Pellet, S.-J. Moon, R. Humphry-Baker, P. Gao, M. K. Nazeeruddin and M. Grätzel, *Nature*, 2013, **499**, 316.

M. M. Lee, J. Teuscher, T. Miyasaka, T. N. Murakami, and H. J. Snaith, *Science*, 2012, **338**, 643.

E. J. Juarez-Perez, R. S. Sanchez, L. Badia, G. Garcia-Belmonte, Y. S. Kang, I. Mora-Sero and J. Bisquert, *J. Phys. Chem. Lett.*, 2014, **5**, 2390.

C. C. Stoumpos, L. Mao, C. D. Malliakas, and M. G. Kanatzidis, *Inorg. Chem.*, 2017, **56**, 56.

Z. Shi, J. Guo, Y. Chen, Q. Li, Y. Pan, H. Zhang, Y. Xia and W. Huang, *Adv. Mater.*, 2017, 1605005.

X.-H. Zhao, X.-C. Huang, S.-L. Zhang, D. Shao, H.-Y. Wei and X.-Y. Wang, *J. Am. Chem. Soc.*, 2013, **135**, 16006.

F. A. Mautner, R. Cortés, L. Lezama and T. Rojo, *Angew. Chem., Int. Ed. Engl.*, 1996, **35**, 78.

Z.-Y. Du, T.-T. Xu, B. Huang, Y.-J. Su, W. Xue, C.-T. He, W.-X. Zhang and X.-M. Chen, *Angew. Chem. Int. Ed.*, 2015, **54**, 914.

Z.-Y. Du, Y.-Z. Sun, S.-L. Chen, B. Huang, Y.-J. Su, T.-T. Xu, W.-X. Zhang and X.-M. Chen, *Chem. Commun.*, 2015, **51**, 15641.

Z.-Y. Du, Y.-P. Zhao, W.-X. Zhang, H.-L. Zhou, C.-T. He, W. Xue, B.-Y. Wang and X.-M. Chen, *Chem. Commun.*, 2014, **50**, 1989.

Z.-Y. Du, Y.-P. Zhao, C.-T. He, B.-Y. Wang, W. Xue, H.-L. Zhou, J. Bai, B. Huang, W.-X. Zhang and X.-M. Chen, *Cryst. Growth Des.*, 2014, **14**, 3903.

L. C. Gómez-Aguirre, B. Pato-Doldán, A. Stroppa, L.-M. Yang, T. Frauenheim, J. Mira, S. Yáñez-Vilar, R. Artiaga, S. Castro-García, M. Sánchez-Andújar and M. A. Señarís-Rodríguez, *Chem. Eur. J.* 2016, **22**, 7863.

W. Zhang, Y. Cai, R.-G. Xiong, H. Yoshikawa and K. Awaga, *Angew. Chem. Int. Ed.*, 2010, **122**, 6758.

X. Zhang, X.-D. Shao, S.-C. Li, Y. Cai, Y.-F. Yao, R.-G. Xiong and W. Zhang, *Chem. Commun.*, 2015, **51**, 4568.

W.-J. Xu, S.-L. Chen, Z.-T. Hu, R.-B. Lin, Y.-J. Su, W.-X. Zhang and X.-M. Chen, *Dalton Trans.*, 2016, **45**, 4224.

C. Shi, C.-H. Yu and W. Zhang, *Angew. Chem. Int. Ed.*, 2016, **55**, 5798.

W. Zhang, H.-Y. Ye, R. Graf, H. W. Spiess, Y.-F. Yao, R.-Q. Zhu and R.-G. Xiong, *J. Am. Chem. Soc.*, 2013, **135**, 5230.

P. Xie, W.-J. Xu, C.-T. He, B. Huang, Z.-Y. Du, Y.-J. Su, W.-X. Zhang and X.-M. Chen, *CrystEngComm*, 2016, **18**, 4495.

G. Thiele and D. Messer, *Z. Anorg. Allg. Chem.*, 1980, **464**, 255.

J. Lefebvre, D. Chartrand and D. B. Leznoff, *Polyhedron*, 2007, **26**, 2189.

J. A. Hill, A. L. Thompson and A. L. Goodwin, *J. Am. Chem. Soc.*, 2016, 138, 5886.

M.-L. Tong, J. Ru, Y.-M. Wu, X.-M. Chen, H.-C. Chang, K. Mochizuki and S. Kitagawa, *New J. Chem.*, 2003, 27, 779.

J. A. Schlueter, J. L. Manson, K. A. Hyzer and U. Geiser, *Inorg. Chem.*, 2004, **43**, 4100.

J. A. Schlueter, J. L. Manson and U. Geiser, *Inorg. Chem.*, 2005, **44**, 3194.

J. M. Bermúdez-García, M. Sánchez-Andújar, S. Yáñez-Vilar, S. Castro-García, R. Artiaga, J. López-Beceiro, L. Botana, A. Alegría and M. A. Señarís-Rodríguez, *Inorg. Chem.*, 2015, **54**, 11680.

J. M. Bermúdez-García, M. Sánchez-Andújar, S. Yáñez-Vilar, S. Castro-García, R. Artiaga, J. López-Beceiro, L. Botana, A. Alegría and M. A. Señarís-Rodríguez, *J. Mater. Chem. C*, 2016, **4**, 4889.

J. M. Bermúdez-García, S. Yáñez-Vilar, A. García-Fernández, M. Sánchez-Andújar, S. Castro-García, J. Mira, J. A. Moreira, T. A. Centeno and M. A. Señarís-Rodríguez, *New J. Chem.*, 2017, **41**, 3124.

F.-J. Geng, L. Zhou, P.-P. Shi, X.-L. Wang, X. Zheng, Y. Zhang, D.-W. Fu and Q. Ye, *J. Mater. Chem. C*, 2017, **5**, 1529.

L. Zhou, X. Zheng, P.-P. Shi, Z. Zafar, H.-Y. Ye, D.-W. Fu and Q. Ye, *Inorg. Chem.*, 2017, **56**, 3238.

J. M. Bermúdez-García, M. Sánchez-Andújar, S. Castro-García, J. López-Beceiro, R. Artiaga and M. A. Señarís-Rodríguez, *Nat. Commun.*, 2017, **8**, 15715.

J. M. Bermúdez-García, M. Sánchez-Andújar and M. A. Señarís-Rodríguez, *J. Phys. Chem. Lett.*, 2017, **8**, 4419.

X. Moya, S. Kar-Narayan and N. D. Mathur, *Nat. Mater.*, 2014, **13**, 439.

X. Moya, E. Defay, V. Heine and N. D. Mathur, *Nat. Phys.*, 2015, **11**, 202.

S. Crossley, N. D. Mathur and X. Moya, *AIP Advances* 2015, **5**, 067153.

Ll. Mañosa and A. Planes, *Adv. Mater.*, 2017, 1603607.

R. C. Arora, *Refrigeration and air conditioning*, PHI Learning Pvt. Ltd, 2012.

H. Hauptman, *Science*, 1986, **233**, 178.

G. M. Sheldrick, *Acta Crystallogr., Sect. A: Cryst. Phys., Diffr., Theor. Gen. Crystallogr.*, 2008, **64**, 112.

L. J. Farrugia, *J. Appl. Cryst.*, 2012, **45**, 849.

A. Le Bail, H. Duroy and J. L. Fourquet, *Mater. Res. Bull.*, 1988, **23**, 447.

J. D. Dudley and H. T. Hall, *Phys. Rev.*, 1960, **118**, 1211.

G. W. H. Höhne, W. Dollhopf, K. Blankenhorn and P. U. Mayr, *Thermochim. Acta*, 1996, **273**, 17.

R. D. Shannon, *Acta Crystallogr., Sect. A: Found. Crystallogr.*, 1976, **32**, 751.

P. Lloveras, E. Stern-Taulats, M. Barrio, J.-Ll. Tamarit, S. Crossley, W. Li, V. Pomjakushin, A. Planes, Ll. Mañosa, N.D. Mathur and X. Moya, *Nat. Commun.*, 2015, **6**, 8801.

A. Aznar, P. Lloveras, M. Romanini, M. Barrio, J.-Ll. Tamarit, C. Cazorla, D. Errandonea, N. D. Mathur, A. Planes, X. Moya and Ll. Mañosa, *Nat. Commun.*, 2017, **8**, 1851.

G. Kieslich, S. Sun and A. K. Cheetham, *Chem. Sci.*, 2014, **5**, 4712.

G. Kieslich, S. Sun and A. K. Cheetham, *Chem. Sci.*, 2015, **6**, 3430.

W. Travis, E. N. K. Glover, H. Bronstein, D. O. Scanlon and R. G. Palgrave, *Chem. Sci.*, 2016, **7**, 4548.

D. Matsunami, A. Fujita, K Takenaka and M. Kano, *Nat. Mater.*, 2015, **14**, 73.

Ll. Mañosa, D. González-Alonso, A. Planes, E. Bonnot, M. Barrio, J.-Ll. Tamarit, S. Aksoy and M. Acet, *Nat. Mater.*, 2010, **9**, 478.

S. Yuce, M. Barrio, B. Emre, E. Stern-Taulats, A. Planes, J.-Ll. Tamarit, Y. Mudryk, K. A. Gschneidner Jr., V. K. Pecharsky, and Ll. Mañosa, *Appl. Phys. Lett.*, 2012, **101**, 071906.

E. Stern-Taulats, A. Planes, P. Lloveras, M. Barrio, J.-Ll. Tamarit, S. Pramanick, S. Majumdar, C. Frontera and Ll. Mañosa, *Phys. Rev. B*, 2014, **89**, 214105.

E. Stern-Taulats, P. Lloveras, M. Barrio, E. Defay, M. Egilmez, A. Planes, J.-LI. Tamarit, Ll. Mañosa, N. D. Mathur and X. Moya, *APL Materials*, 2016, **4**, 091102.

I. N. Flerov, V. D. Fokina, A. F. Bovina, E. V. Bogdanov, M. S. Molokeev, A. G. Kocharova, E. I. Pogorel'tsev and N. M. Laptash, *Phys. Solid State*, 2008, **50**, 515.